Validation of Multi-Body Modelling Methodology for Reconfigurable Underwater Robots

M.C. Nielsen[1,2], O. A. Eidsvik[3], M. Blanke[1,2] and I. Schjølberg[3]

***Abstract*—This paper investigates the problem of employing reconfigurable robots in an underwater setting. The main results presented is the experimental validation of a modelling methodology for a system consisting of N dynamically connected robots with heterogeneous dynamics. Two distinct types of experiments are performed, a series of hydrostatic free-decay tests and a series of open-loop trajectory tests. The results are compared to a simulation based on the modelling methodology. The modelling methodology shows promising results for usage with systems composed of reconfigurable underwater modules. The purpose of the model is to enable design of control strategies for cooperative reconfigurable underwater systems.**

I. Introduction

The offshore industry is technologically demanding with a strong focus on sustainable production. Offshore production facilities are moving from the surface of the sea to the sea floor to save costs and energy. As a result, robotic solutions are employed for performing an increasing variety of tasks, such as inspection, maintenance and repair (IMR). Under this prism, cooperation and reconfiguration of robotics systems are anticipated to become essential tools for such a technological development. Reconfiguration pertains to the ability for a set of robots to physically assume different relative configurations in order to form a larger robotic system. Variation in the configuration of these connections results in vastly different dynamics for the combined system. This paper addresses the experimental validation of a modelling approach for a system of interconnected underwater robots given the dynamics of each individual module.

Current solutions focus on Remotely-Operated-Vehicles (ROVs) for high-power operations, such as positioning subsea modules during installation [1]. However, for low-power operations and in cluttered environments an autonomous and tether-free solution is preferable due to risk of entanglement of the connecting cable. In the long term a modular reconfigurable multi-robot solution can provide higher operational flexibility for solving a number of complex IMR operations.

Reconfiguration is a broad topic and has been investigated in several different contexts such as self-assembly of large maritime structures [2]. For underwater applications the assembly of heterogeneous robots is investigated in relation to data-retrieval of underwater sensor networks [3]. Docking with the purpose of assembly for small-sized autonomous underwater vehicles (AUVs) was also investigated in relation to homogeneous robots in [4]. For most control strategies, the first important step is to procure a mathematical model that adequately describes the dynamic behaviour of the system. Modelling of generic underwater vehicles has been treated extensively in the literature such as in [5] and [6]. However, modelling of reconfigurable underwater systems has not previously been investigated. Hej Similarly to the case of generic underwater systems, the process of modelling a reconfigurable system becomes more complex due to the non-linearities that

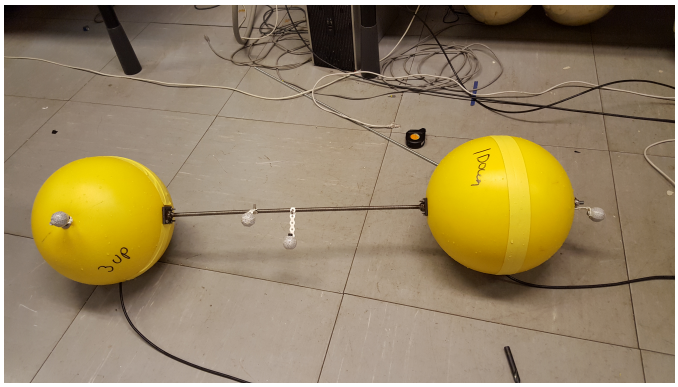

(a) Hydrostatic Configuration: Two identical modules connected in relative attitude to each other by a rigid rod.

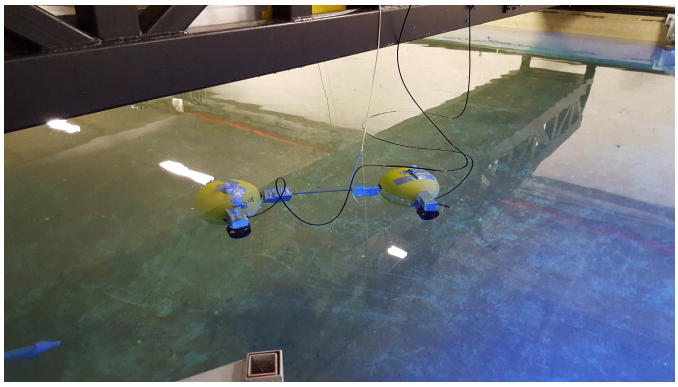

(b) Hydrodynamic Configuration: Two identical modules a thruster connected to eeach other by a rigid rod.

Fig. 1: The two experimental configurations used in the validation procedure.

[1] Centre for Autonomous Operations and Systems, Department of Cybernetics, Norwegian University of Science and Technology, Trondheim, Norway
[2] Department of Electrical Engineering, Technical University of Denmark, Lyngby, Denmark
[3] Centre for Autonomous Operations and Systems, Department of Marine Technology, Norwegian University of Science and Technology, Trondheim, Norway

arise from the hydrodynamics. Furthermore, reconfiguration is envisioned to occur during operation and therefore renders Computational-Fluid-Dynamic (CFD) methods infeasible for estimating the system parameters at every configuration change.

Multi-body dynamics for underwater applications has been investigated in multiple papers. An application of these methods for an underwater system is presented in [7] and [8], where the dynamics of the tether cables are studied. More recently, multi-body dynamics methods have been used for modelling AUVs [9], [10], [11] and [12].

The contribution of this paper is testing and verification of a dynamic model for systems of interconnected reconfigurable underwater robotic modules. The modelling approach is based on an application of the Udwadia-Kalaba Equation as presented [13]. The testing and verification of the dynamic model is performed through experiments in a wet lab and the results are compared with simulations. The system applied in the experiments consists of two spheric objects with thrusters interconnected by a rod. Two types of experiments are performed; one hydrostatic experiments where only the restoring forces act on the system as seen in Fig. 1a and one hydrodynamic experiments, where both modules have thrusters mounted as seen in Fig. 1b. This represents the dynamics of to thrustered underwater robots carrying an underwater module in an maintenance operation.

The paper starts by listing the notation, kinematics and kinetics used in the modelling approach. Section III then describes the modelling methodology. Then in Section IV the approach to identifying the individual model for each robot in the network is described, leading to Section V where the experimental setup is documented and explained. The results of the experimental trails are presented in Section VI. The validity of the results is discussed in Section VII. Finally in Section VIII conclusions are drawn and future work is discussed.

II. Rigid-Body Modelling

This section provides the notation used throughout the paper along with the kinematics and dynamics governing each rigid body.

A. Notation and Kinematics

The kinematics are formulated in two different reference frames, a global and a local frame. For the global reference frame, the earth-fixed North-East-Down (NED) frame denoted by $\{n\}$ is used and assumed inertial. The configuration of each rigid-body in the global frame is defined by the position and the attitude with respect to the frame such that $\boldsymbol{\eta} = [\boldsymbol{p}^n_{b/n}, \boldsymbol{u}]^T \in \mathbb{R}^7$ comprise of the position $\boldsymbol{p}^n_{b/n} = [x^n, y^n, z^n]^T$ and the attitude represented as a unit quaternion to avoid singularities $\boldsymbol{u} = [\eta, \varepsilon_1, \varepsilon_2, \varepsilon_3]^T$. The local frame of reference is a moving reference frame fixed to each rigid body in the system. The local-body fixed coordinate frame is denoted by $\{b\}$. Velocities are conveniently expressed in the body-frame and denoted $\boldsymbol{\nu}$ as shown below

$$\boldsymbol{\nu} = \begin{bmatrix} u & v & w & p & q & r \end{bmatrix}^T \in \mathbb{R}^6 \tag{1}$$

The body-fixed velocities can be divided into linear velocities $\boldsymbol{v}^b_{b/n} = [u, v, w]^T$ and angular velocities $\boldsymbol{\omega}^b_{b/n} = [p, q, r]^T$. The local body-fixed frames are related to the global frame through a rotation matrix $\boldsymbol{R}^n_b$ defined below

$$\boldsymbol{R}^n_b = \begin{bmatrix} 1-2\left(\varepsilon_2^2+\varepsilon_3^2\right) & 2\left(\varepsilon_1\varepsilon_2-\varepsilon_3\eta\right) & 2\left(\varepsilon_1\varepsilon_3+\varepsilon_2\eta\right) \\ 2\left(\varepsilon_1\varepsilon_2+\varepsilon_3\eta\right) & 1-2\left(\varepsilon_1^2+\varepsilon_3^2\right) & 2\left(\varepsilon_2\varepsilon_3-\varepsilon_1\eta\right) \\ 2\left(\varepsilon_1\varepsilon_3-\varepsilon_2\eta\right) & 2\left(\varepsilon_2\varepsilon_3+\varepsilon_1\eta\right) & 1-2\left(\varepsilon_1^2+\varepsilon_2^2\right) \end{bmatrix} \tag{2}$$

The attitude change in the global frame $\{n\}$ is related to the angular velocities $\boldsymbol{\omega}^b_{b/n}$ in the body-fixed frame $\{b\}$ through the angular transformation matrix $\boldsymbol{T}_u$ defined below

$$\dot{\boldsymbol{u}} = \boldsymbol{T}_u \boldsymbol{\omega}^b_{b/n} \tag{3}$$

where $\boldsymbol{T}_u$ is defined as

$$\boldsymbol{T}_u = \frac{1}{2}\boldsymbol{H}^T = \frac{1}{2}\begin{bmatrix} -\varepsilon_1 & -\varepsilon_2 & -\varepsilon_3 \\ \eta & -\varepsilon_3 & \varepsilon_2 \\ \varepsilon_3 & \eta & -\varepsilon_1 \\ -\varepsilon_2 & \varepsilon_1 & \eta \end{bmatrix} \tag{4}$$

such that $\boldsymbol{H}$ is

$$\boldsymbol{H} = \begin{bmatrix} -\boldsymbol{\varepsilon} & \eta\boldsymbol{I}_3 - \boldsymbol{S}(\boldsymbol{\varepsilon}) \end{bmatrix} \in \mathbb{R}^{3\times 4} \tag{5}$$

where $\boldsymbol{S}(\boldsymbol{\varepsilon})$ is the skew-symmetric matrix such that $\boldsymbol{S}(\boldsymbol{\lambda})^T = -\boldsymbol{S}(\boldsymbol{\lambda})$ and it is defined as

$$\boldsymbol{S}(\boldsymbol{\lambda}) = \begin{bmatrix} 0 & -\lambda_3 & \lambda_2 \\ \lambda_3 & 0 & -\lambda_1 \\ -\lambda_2 & \lambda_1 & 0 \end{bmatrix} \tag{6}$$

Through a small modification to the $\boldsymbol{H}$ matrix the angular velocities of the body fixed frame represented can be related to the attitude representation in the global frame.

$$\bar{\boldsymbol{H}} = \begin{bmatrix} -\boldsymbol{\varepsilon} & \eta\boldsymbol{I}_3 + \boldsymbol{S}(\boldsymbol{\varepsilon}) \end{bmatrix} \in \mathbb{R}^{3\times 4} \tag{7}$$

$$\dot{\boldsymbol{u}} = \bar{\boldsymbol{T}}_u \boldsymbol{\omega}^n_{b/n} \tag{8}$$

The linear and angular transformation matrices can be combined into a combined transformation matrix $\boldsymbol{J}_u$ as shown below

$$\boldsymbol{J}_u = \begin{bmatrix} \boldsymbol{R}^n_b & \boldsymbol{0}_{3\times 3} \\ \boldsymbol{0}_{4\times 3} & \boldsymbol{T}_u \end{bmatrix} \tag{9}$$

In underwater applications the current velocity is the primary disturbance. To include the current in the model formulation the approach in [6] is taken such that the velocities are described in relative velocity. Under the following assumption the relative velocity vector can be written as $\boldsymbol{\nu}_r = \boldsymbol{\nu} - \boldsymbol{\nu}_c$ where $\boldsymbol{\nu}_c$ is the velocity of the water current in the body-fixed frame.

Assumption 1: The current is constant and irrotational in the inertial frame.

Assumption 1 is reasonable in the sense that both amplitude and direction of currents are slowly varying.

B. Dynamics

The kinetic model used for the individual module in relative velocities is described in [6] and will be restated here for completeness.

Assumption 2: The fluid is viscid, incompressible and irrotational.

Assumption 2 is common in hydrodynamic modelling. Hence the model used in this paper is stated below

$$\boldsymbol{M}\dot{\boldsymbol{\nu}}_r + \boldsymbol{D}\left(\boldsymbol{\nu}_r\right)\boldsymbol{\nu}_r + \boldsymbol{C}\left(\boldsymbol{\nu}_r\right)\boldsymbol{\nu}_r + \boldsymbol{g}\left(\boldsymbol{\eta}\right) = \boldsymbol{\tau} \tag{10}$$

Claim 1: Parasitic hydrodynamic forces arising from proximity of other modules are not dominant compared to the individual modules own dynamics.

Claim 1 is the basis for our model investigation. This concludes the section on notation, kinematics and kinetics. The following section will present the multi-body dynamics modelling methodology and the necessary constraint equation used to describe the combined system.

III. Multi-Body Dynamics

This section will provide the theoretical background for the modelling method as was presented in [13].

A. Udwadia-Kalaba Equation

The work is based on the work in [14] where the general Udwadia-Kalaba formulation was extended to include quasi-velocities and quasi-accelerations. To avoid confusion of subscripts an auxiliary set of variables are used and tied to our defined notation in the end of the section. Consider a transformation $\boldsymbol{G}\left(\boldsymbol{q}\right) \in \mathbb{R}^{n_s \times n_q}$ such that

$$\boldsymbol{s} = \boldsymbol{G}\left(\boldsymbol{q}\right)\dot{\boldsymbol{q}} \tag{11}$$

where $\boldsymbol{s} \in \mathbb{R}^{n_s}$ is a vector of quasi-velocities, $\boldsymbol{q} \in \mathbb{R}^{n_q}$ is the vector of generalised coordinates and $\dot{\boldsymbol{q}}$ is the vector of generalised velocities. An unconstrained Newtonian mechanical system can be formulated in terms of quasi-coordinates as shown below

$$\boldsymbol{M}\dot{\boldsymbol{s}}_u = \boldsymbol{S} \tag{12}$$

where $\boldsymbol{M} \in \mathbb{R}^{n_s \times n_s}$ is the inertia matrix, $\dot{\boldsymbol{s}}_u$ is the vector of unconstrained quasi-accelerations and $\boldsymbol{S} \in \mathbb{R}^{n_s}$ is the generalised forces in the frame where the quasi-coordinates are defined.

Subjecting the unconstrained system to a constraint imposes an additional force and hence the formulation in Eq. 12 can be re-formulated to include a constraining force $\boldsymbol{S}_c \in \mathbb{R}^{n_s}$ as shown below

$$\boldsymbol{M}\dot{\boldsymbol{s}}_c = \boldsymbol{S} + \boldsymbol{S}_c \tag{13}$$

The problem of constrained dynamics is to identify the constraining force vector $\boldsymbol{S}_c$. There exists numerous ways to identify or otherwise compensate for the constraint in the system. The Udwadia-Kalaba Equation calculates the constraint force and compensates the motion on the force level. In order to do so the constraint must be able to be expressed linearly in the accelerations. That is given n_c constraints the constraints must follow the linear relationship stated below

$$\boldsymbol{A}\left(\boldsymbol{q}, \boldsymbol{s}\right)\dot{\boldsymbol{s}} = \boldsymbol{b}\left(\boldsymbol{q}, \boldsymbol{s}\right) \tag{14}$$

where $\boldsymbol{A} \in \mathbb{R}^{n_c \times n_s}$ is the constraint matrix and $\boldsymbol{b} \in \mathbb{R}^{n_c}$ is the constraint vector.

The Udwadia-Kalaba Equation solves the constraint force by transforming the problem into an optimisation problem using Gauss' Principle of Least Constraint as explained in [15]. Hence, the problem of handling the constraints becomes a minimisation problem which is then solved by using the Moore-Penrose pseudo-inverse. Thereby the constraint force vector $\boldsymbol{S}_c$ can be expressed as below

$$\boldsymbol{S}_c = \boldsymbol{M}^{1/2}\Big(\boldsymbol{A}\boldsymbol{M}^{-1/2}\Big)^{+}\left(\boldsymbol{b} - \boldsymbol{A}\dot{\boldsymbol{s}}_u\right) \tag{15}$$

where $(\cdot)^{+}$ represents the Moore-Penrose pseudo-inverse. The identified constraint force vector $\boldsymbol{S}_c$ is then used to compensate the constrained system equations of Eq. (13) such that the constrained acceleration $\dot{\boldsymbol{s}}_c$ can be found as shown below

$$\dot{\boldsymbol{s}}_c = \dot{\boldsymbol{s}}_u + \boldsymbol{M}^{-1/2}\Big(\boldsymbol{A}\boldsymbol{M}^{-1/2}\Big)^{+}\left(\boldsymbol{b} - \boldsymbol{A}\dot{\boldsymbol{s}}_u\right) \tag{16}$$

Since the Udwadia-Kalaba Equation requires global formulation the quasi-velocity vector $\boldsymbol{s}$ corresponds a vector of all the body-fixed frame velocities in the system.

$$\boldsymbol{s} = \begin{bmatrix}\boldsymbol{\nu}_1, \boldsymbol{\nu}_2, \ldots, \boldsymbol{\nu}_N\end{bmatrix}^T \tag{17}$$

where the subscript denotes the vehicle. The transformation matrix $\boldsymbol{G}(\boldsymbol{q})$ represents the transformation from global to local coordinates and in the same way as with the quasi-velocities is defined for the combined system ie. $\boldsymbol{G}(\boldsymbol{q})$ is block diagonal matrix with $\boldsymbol{J}_{u_i}^T$ for $i \in \{1, \ldots, N\}$ in the diagonal as shown below

$$\boldsymbol{G}(\boldsymbol{q}) = \begin{bmatrix} \boldsymbol{J}_{u_1}^T & \boldsymbol{0}_{7\times 6} & \ldots & \boldsymbol{0}_{7\times 6} \\ \boldsymbol{0}_{7\times 6} & \boldsymbol{J}_{u_2}^T & \ddots & \vdots \\ \vdots & \ddots & \ddots & \vdots \\ \boldsymbol{0}_{7\times 6} & \cdots & \cdots & \boldsymbol{J}_{u_N}^T \end{bmatrix} \tag{18}$$

By definition the generalised coordinates $\boldsymbol{q}$ are the global configuration of the system.

$$\boldsymbol{q} = \begin{bmatrix}\boldsymbol{\eta}_1, \boldsymbol{\eta}_2, \ldots, \boldsymbol{\eta}_N\end{bmatrix}^T \tag{19}$$

In many robotic applications quasi-velocities are advantageous compared to generalised velocities. In [16] the Udwadia-Kalaba formulation was used to model a system of N multi-copters for the purpose of slung-load transportation using local coordinates.

B. Constraint Equation

As was explained in previous subsection, the constraints are required to be represented linearly in the quasi-accelerations. The constraint type pursued in this paper is a rigid connection between the robots defined on the configuration level. The constraint can be split into a positional and attitude constraint as shown below

$$\boldsymbol{c}_1 \ : \ \boldsymbol{p}^n_{A/n} + \boldsymbol{p}^n_{s/A} - \boldsymbol{p}^n_{B/n} - \boldsymbol{p}^n_{s/B} = 0 \tag{20}$$

$$\boldsymbol{c}_2 \ : \ \boldsymbol{u}_A \otimes \boldsymbol{u}^*_B = \boldsymbol{u}_{rel} \tag{21}$$

where $\otimes$ is the Hamilton product between the quaternions. The derivation of the constraint matrix $\boldsymbol{A}$ and the constraint vector $\boldsymbol{b}$ to acceleration level is described in [13] and hence only the result and main points are given here. For the positional constraint $\boldsymbol{c}_1$ between two vehicles A and B the $\boldsymbol{A}_1$ matrix is shown below

$$\boldsymbol{A}_1 = \begin{bmatrix} \boldsymbol{R}^n_A & -\boldsymbol{S}(\boldsymbol{p}^n_{s/A}) & -\boldsymbol{R}^n_B & \boldsymbol{S}(\boldsymbol{p}^n_{s/B}) \end{bmatrix} \in \mathbb{R}^{3\times 12} \tag{22}$$

The constraint vector $\boldsymbol{b}_1$ becomes

$$\begin{aligned} \boldsymbol{b}_1 = &-\boldsymbol{\omega}^n_{A/n} \times (\boldsymbol{R}^n_A \boldsymbol{\nu}^{(A)}_r + \boldsymbol{\omega}^n_{A/n} \times \boldsymbol{p}^n_{s/A}) \\ &+ \boldsymbol{\omega}^n_{B/n} \times (\boldsymbol{R}^n_B \boldsymbol{\nu}^{(B)}_r + \boldsymbol{\omega}^n_{B/n} \times \boldsymbol{p}^n_{s/B}) \end{aligned} \tag{23}$$

Similarly conducting the double derivative and re-writing terms for the attitude constraint $\boldsymbol{c}_2$ between the two vehicles denoted A and B yields

$$\boldsymbol{A}_2 = \begin{bmatrix} \boldsymbol{0}_{4\times 3} & \boldsymbol{G}_B \boldsymbol{T}_A & \boldsymbol{0}_{4\times 3} & \boldsymbol{G}_A \boldsymbol{T}_B \end{bmatrix} \in \mathbb{R}^{4\times 12} \tag{24}$$

$$\boldsymbol{b}_2 = -\boldsymbol{G}_A \dot{\boldsymbol{T}}_B \boldsymbol{\omega}^B_{B/n} - \left(\boldsymbol{G}_B \dot{\boldsymbol{T}}_A + 2\dot{\boldsymbol{G}}_B \boldsymbol{T}_A \right) \boldsymbol{\omega}^A_{A/n} \tag{25}$$

where $\boldsymbol{G}_A$ is a matrix of elements from the quaternion of vehicle A as shown below

$$\begin{aligned} \boldsymbol{u}_A \otimes \boldsymbol{u}^*_B &= \begin{bmatrix} (\boldsymbol{u}_B)^T \\ \bar{\boldsymbol{H}}_B \end{bmatrix} \boldsymbol{u}_A = \boldsymbol{G}_B \boldsymbol{u}_A \\ &= \begin{bmatrix} (\boldsymbol{u}_A)^T \\ -\bar{\boldsymbol{H}}_A \end{bmatrix} \boldsymbol{u}_B = \boldsymbol{G}_A \boldsymbol{u}_B \end{aligned} \tag{26}$$

This concludes the presentation of the modelling methodology and the rigid constraint formulation.

IV. Parametric Identification

The modelling methodology described in this paper revolve around the individual model to produce the overall behaviour. This section describes which procedure was used to acquire the necessary parameters of the individual robots.

Assumption 3: In this paper each module will be assumed to have 3 planes of symmetry.

While it is rarely the case that vehicles exhibit 3 planes of symmetry Assumption 3 is fairly common for underwater vehicles and conveniently allows the drag and added mass for the individual module to be described as diagonal matrices.

Assumption 4: The vehicles are submerged far below the free surface.

Assumption 4 removes the frequency dependent potential damping and further simplifies the individual model description. Hence, the total drag force for each degree of freedom can approximated as a linear and quadratic term shown below [6].

$$D(v) = D_L v + D_Q |v| v \tag{27}$$

The diagonal elements of the damping matrices are determined numerically by CFD using SolidWorks Flow Simulation using the Morison equation below

$$f(v) = \underbrace{\frac{1}{2} C_d \rho A}_{D_Q} v^2 \tag{28}$$

where C_d is the drag coefficient, A is the cross-section of the vehicle, v is the velocity of the fluid across the surface, $f(v)$ is the drag force as a function of the velocity and D_Q is a collective term for the quadratic drag. The problem of determining the linear skin friction is discussed in **Eidsvik2016** where the author proposes to approximate it using the scaled quadratic drag as was done in **Eng2008** For the translational degrees of freedom the following relation is used

$$D_L = 0.16 D_Q \tag{29}$$

For the rotational degrees of freedom the authors use the following relation based on [6].

$$D_L = 2\xi m \sqrt{\frac{r}{m + m_a}} \tag{30}$$

where ξ is a damping factor in the region $2\% - 10\%$, m is the mass of the vehicle, m_a is the added mass and r is the restoring force. The restoring force r is the result of the restoring force vector $\boldsymbol{g}(\boldsymbol{\eta})$. Using the Computer-Aided-Design (CAD) model of the vehicles the centre of buoyancy (CB) is determined to lie vertically above the centre of gravity (CG). Hence, the restoring force vector $\boldsymbol{g}(\boldsymbol{\eta})$ can be described as below [6].

$$\boldsymbol{g}(\boldsymbol{\eta}) = [0, 0, 0, \overline{BG}_z W \cos(\theta)\sin(\phi), \overline{BG}_z \sin(\theta)\cos(\phi), 0]^T \tag{31}$$

where $\overline{BG}_z$ is the vertical distance from CG to CB and W is the weight of the vehicle. Since yaw has no restoring force the authors in **Eidsvik2016** use the following relation

$$N_r \approx \frac{K_p}{K_{|p|p}} N_{|r|r} \tag{32}$$

where N_r is the linear drag coefficient for the yaw-axis, K_p is the linear drag coefficient of the roll-axis, $K_{|p|p}$ is the quadratic drag of the roll-axis and $N_{|r|r}$ is the quadratic drag of the yaw-axis following the SNAME[1] notation.

V. Experimental Setup

This section outlines and explains three experiments conducted to validate the modelling methodology. Two experiments are considered, first a hydrostatic experiment is conducted where two identical modules are connected by a rigid rod in a

[1] Society of Naval Architects and Marine Engineers

relative attitude as shown on Fig. 4a and 1a, where module B is mounted on module A in 90° relative roll. Secondly a hydrodynamic experiment is conducted, where each module is retrofitted with a BlueRobotics T-200 thruster to actuate the system and mounted to each other by a rigid rod with zero relative attitude as shown in Fig. 4b and 1b. To facilitate a simulation for the hydrodynamic case the thrusters must be identified which leads to the third experiment which is static thruster tests.

A. Hydrostatic Experiment

The purpose of the hydrostatic test is to investigate the interaction between the two bodies under influence of only the gravity vector $\boldsymbol{g}$ without any actuation $\boldsymbol{\tau} = 0$ and identical hydrodynamic profiles. In Fig. 2 the rod used to connect the vehicles is shown along with a measuring tape. The length of the rod l_r was measured to be $596mm$ and the weight of the rod was $500g$.
To induce a restoring force moment on the system the vehicles are attached to each other in a relative attitude. In this case vehicle B was attached to vehicle A in a relative attitude of 90° around the local x_B-axis (roll). In Fig. 4a this corresponds to the red vehicle where $\phi_{rel} = 90^\circ$. Ideally, the CB of vehicle A and B is placed at CB_A and CB_B respectively.

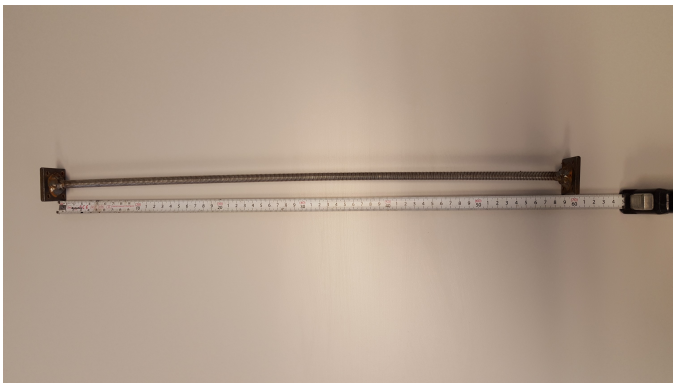

Fig. 2: Connecting rod with a measuring tape. By inspection the length of the rod is determined to be $l_r = 596mm$.

B. Hydrodynamic Experiment

In the hydrodynamic experiment a thruster is mounted on each vehicle to apply a force. To isolate the motion induced by the thrusters the configuration of the robots are changed such the relative attitude for each vehicle is zero. The experimental configuration is shown in Fig. 4b. Hence, the actuation is no longer zero $\boldsymbol{\tau}_i \neq \mathbf{0}$ for $i \in \{A, B\}$. Two configurations are considered, first by using identical vehicles the expected trajectory of the combined CG is a straight line. Secondly by reducing the size of vehicle B the trajectory is expected to diverge towards the port side.

C. Thruster Characteristics

In order to conduct the hydrodynamic experiments it is necessary to know the thruster characteristics. The thrusters used in the experiments are the T-200 thruster from BlueRobotics. Open water performance charts are available on their product page[2]. However, the thrusters for the experiments are mounted in close proximity of the hull of the robots. Thus, the flow is reduced and therefore the force exerted by the thruster is reduced.
To measure this each of the two sized vehicles are mounted on a bracket as shown in Fig. 3 and lowered into the water. Three load cells were attached between the mounting bracket and the bridge.

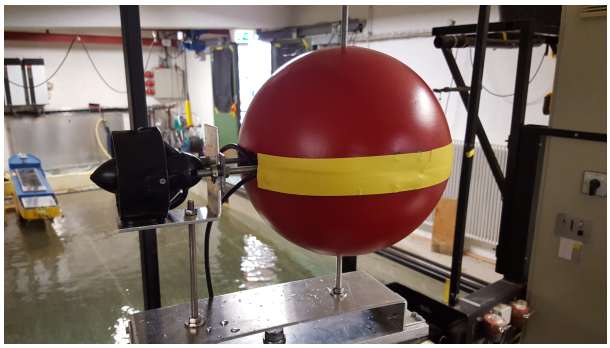

Fig. 3: Small sized robot with thruster secured to bracket.

VI. Results

The experiments were performed in Marine Cybernetics Laboratory (MCLAB) at NTNU in Trondheim. The tracking system used to monitor the motion of the vehicles was a Qualisys Motion Capture system with 6 underwater cameras. The motion data interfaced with the Robot-Operating-System (ROS) middleware and data was acquired at 250 Hz.

A. Hydrostatic Experiment

The hydrostatic experiments were performed by fully submerging the connected robots into the water and position the connecting rod parallel to the water surface. The markers used by the tracking system were strategically attached to allow best possible detection. The parameters used for the comparative simulation are shown in Table I. Upon initialising the motion data capture, the system was released, and the restoring forces began acting [3]. The experiments were conduct 5 times and a comparison between the simulation and one of the data sets is shown in Fig. 5. From the Figure it is clear that the simulation and acquired data is in good agreement. It is noted that the influence of the connecting rod is minimal, seen from the fact that the oscillation period match very well between simulation and experiment, even though the connecting rod is assumed

[2]T-200 performance chart: http://goo.gl/JXcQpy
[3]Video of a hydrostatic experimental run: https://youtu.be/LIwqB7WIbFE

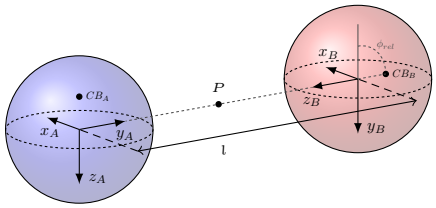

(a) Hydrostatic Test Configuration: Vehicle B is rotated relative to vehicle A by ϕ_{rel} such that axis y_A and z_B coincide.

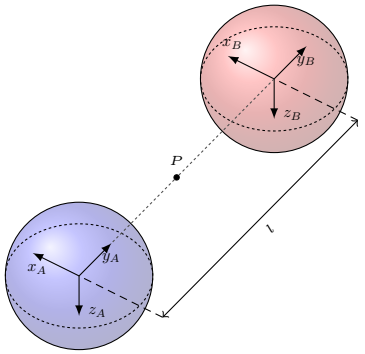

(b) Hydrodynamic Test Configuration: The attitude of both vehicles are identical such that axis y_A and y_B coincide.

Fig. 4: Two configurations containing two vehicles denoted A and B. In both configurations vehicle A is colored blue and vehicle B is colored red.

TABLE I: Parameters used for the hydrostatic simulation

$X_{\|u\|u}$	$Y_{\|y\|y}$	$Z_{\|w\|w}$	$K_{\|p\|p}$	$M_{\|q\|q}$	$N_{\|r\|r}$
3.8	3.8	3.8	0.0082	0.0082	0.0082
X_u	Y_y	Z_w	K_p	M_q	N_r
0.67	0.67	0.67	0.048	0.048	0.048
$X_{\dot{u}}$	$Y_{\dot{y}}$	$Z_{\dot{w}}$	$K_{\dot{p}}$	$M_{\dot{q}}$	$N_{\dot{r}}$
7.06	7.06	7.06	0	0	0
I_{xx}	I_{yy}	I_{zz}	ξ	$\overline{BG}_z$	m
0.13	0.16	0.15	0.02	-0.0114	14

massless in the simulation.

The damping of the system is slightly off in both the beginning of the sequence and at the end, which suggests that quadratic drag is not large enough in the simulation and the linear damping coefficient is lower than indicated by Eq. (29).

To evaluate the fit between simulation and data the mean

TABLE II: Mean Square Error between simulation and data

Run	1	2	3	4	5
MSE	0.002	0.0042	0.0038	0.0154	0.0064

square error is listed in Table II showing a good fit between simulation and experiment.

B. Hydrodynamic Experiment

In the hydrodynamic experiments each module is retrofitted with a thruster. In Table III the new parameters for the vehicles

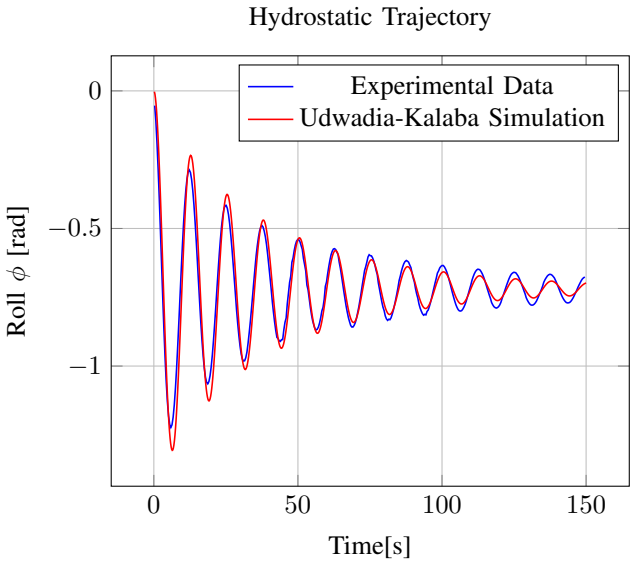

Fig. 5: The figures shows a comparative plot between one pass of the hydrostatic experiments and a simulated counterpart.

with thrusters included are shown. It is worth noticing that the

TABLE III: Parameters used for the hydrodynamic simulation with identical bodies

$X_{\|u\|u}$	$Y_{\|y\|y}$	$Z_{\|w\|w}$	$K_{\|p\|p}$	$M_{\|q\|q}$	$N_{\|r\|r}$
3.8	18.9	12.1	0.0082	0.05	0.108
X_u	Y_y	Z_w	K_p	M_q	N_r
0.61	3	1.9	0.05	0.0353	0.0764
$X_{\dot{u}}$	$Y_{\dot{y}}$	$Z_{\dot{w}}$	$K_{\dot{p}}$	$M_{\dot{q}}$	$N_{\dot{r}}$
6.49	8.1	7.41	0.0074	0.0317	0.0453
I_{xx}	I_{yy}	I_{zz}	ξ	$\overline{BG}_z$	m
0.13	0.16	0.16	0.02	-0.0114	14.3

surge damping $X_{|u|u}$ is estimated to be only 20% of that of a pure sphere. Modelling flow-separation is challenging and the reduced surge damping could be the result of this. The results of a step on both thrusters are shown in Fig. 6. Due to a combination of misalignment in the thrusters mounted on the modules and inaccuracies in the tracking marker placements, the resulting trajectory of the modules were not matching the simulation results. This part of the experiment is therefore going to be repeated.

C. Thruster Characteristics

The thrust tests were conduct by initialise capturing data when no thrust was commanded and then progressively increase the pulse of the Pulse-With-Modulation (PWM) signal to the thrusters. Each step in PWM was kept for 30 seconds starting from 1500 PWM up until 1700 PWM. The load-cells were rated for 18kg and measurements were sampled at 200 Hz. As the load-cell ratings were much larger than the magnitude of the force in question the measurements had low resolution and high noise. The data was post-processed by applying a

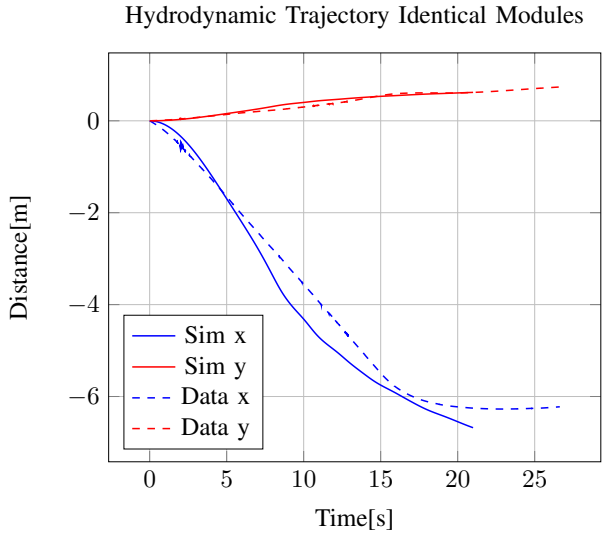

Fig. 6: Hydrodynamic Trajectory of two identical modules

6th order Butterworth low-pass filter and a mean filter with a windows size of 500. The mean of each step plateau was then used as a data sample for the thruster characteristics. The result is shown in Fig. 7. The two data sets share the same

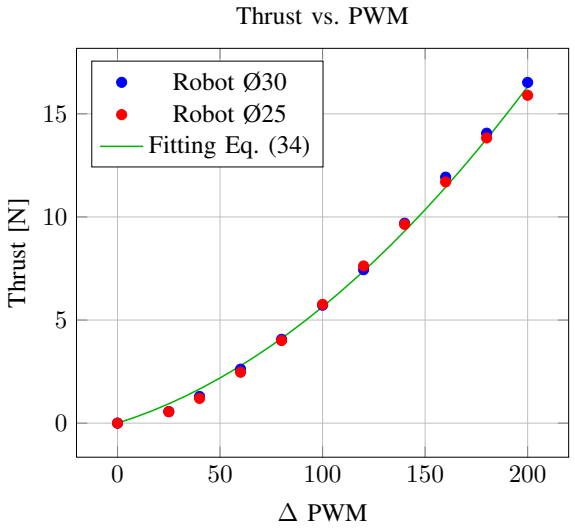

Fig. 7: Thrust Characteristics for two sizes of robots and the PWM to thrust fitting.

profile, this makes sense since the most significant inhibitor of flow to the propeller is the thruster mount which is identical across the two vehicles. The thrust exerted by the thruster is usually modelled as a function of the rotational velocity of the propeller as

$$f = K_T \rho D^4 |n| n \tag{33}$$

where n is the rotational velocity of the propeller in revolutions-per-second (rps), D is the diameter of the propeller, ρ is the water density and K_T is the non-dimensional propeller thrust coefficient. However, from Fig. 7 it is clear that the characteristics is not purely quadratic and thus in this paper the following fitting will be used instead

$$f = K_n n + K_{|n|n} |n| n \tag{34}$$

As the T-200 thruster does not have a way to measure the rotational velocity, a linear relationship is assumed between the rotational velocity and the ΔPWM command. The thrust

TABLE IV: Result of least-square fitting on thrust data on Eq. (34)

K_L	K_Q	R^2
3.123×10^{-2}	2.52×10^{-4}	0.992

data from Fig. 7 was fitted to Eq. (34) using a least-squares and the resulting fit is shown in Tab. IV.

VII. Discussion

The experiments were performed at low velocities where the damping is dominated by linear drag, at higher velocities non-linear damping would influence the results. Furthermore, the distance between the modules in the experiment was large enough such that proximity induced interaction was minimal. The cross-section of the connecting rod was very small compared to the modules themselves, this was done to minimize the influence of the rod. In a realistic scenario, however, the connecting structure would be larger to obtain sufficient strength. As the hydrodynamic experiments showed, inaccuracies in the thruster positions contributed to discrepancies between experiment and simulation. The forces induced on the hull during tests were high enough that warping was apparent. Furthermore, the tracking system coordinate frame attached to the modules was initialised with an unknown offset in the hydrodynamic experiments, which made comparison between experiments and simulations difficult. Finally, modelling flow-separation for a spherical object is challenging, and hence the drag coefficient estimated based on CFD is subject to inaccuracies in this scenario. This is evident from Tab. III where the sway damping is estimated to be slightly larger than for a pure sphere, which is natural due to the thruster and mount, the surge damping, however, is estimated to be around 20% of that of a sphere, which obviously is too low.

A. Improvements

The experiments could be improved by increasing the velocities of the vehicles and reducing the length of the connecting rod. This would strengthen the validity of the modelling approach since in any realistic application of dynamical reconfiguration the mounting port would have larger cross-section than the threaded rod in this experiment. Moreover, the construction of the modules proved too weak for some of the experiments and a future design should incorporate a stronger frame. This would also help to rectify the problem of thruster misalignment.

VIII. Conclusions

This paper presented a method for testing and verification of a modelling methodology for systems of interconnected reconfigurable underwater robotic modules. The experiments shows that the mathematical model is robust with regards to hydrostatic and hydrodynamics properties for the two test cases. In the hydrostatic tests the modules were almost ideally spherical in shape and this was reflected in the results by obtaining a good match between acquired data and the performed simulation. In the hydrodynamic case, inaccuracies in the thruster positions and tracking system precluded the results. The experiments verify the method proposed for dynamic modelling of interconnected reconfigurable underwater modules.

A. Future Work

The contribution of the paper was to show that a reconfigurable underwater robotics system, where the hydrodynamical properties of each module in the system were sufficiently simple, could be modelled adequately using the Udwadia-Kalaba Equation. Future research efforts will be directed towards ROV type vehicles exhibiting more complex hydrodynamic properties. Moreover, during the data processing, the authors noticed that the results were sensitive to certain parameters. Future effort will look into quantifying the sensitivity for the parametric analysis especially considering the uncertainties that often occur in empirical experiments.

Acknowledgement

*This work was supported by the Research Council of Norway through the Centres of Excellence funding scheme, the AMOS project, grant number 223254

References

[1] E. H. Henriksen, T. Berge Gjersvik, and B. Thorkildsen, "Positioning of subsea modules using an automated rov," in *OCEANS 2015 - Genova*, IEEE, 2015, pp. 1–8.

[2] J. Paulos, N. Eckenstein, T. Tosun, J. Seo, J. Davey, J. Greco, V. Kumar, and M. Yim, "Automated self-assembly of large maritime structures by a team of robotic boats," *IEEE Transactions on Automation Science and Engineering*, pp. 1–11, 2015.

[3] I. Vasilescu, K. Kotay, D. Rus, M. Dunbabin, and P. Corke, "Data collection, storage, and retrieval with an underwater sensor network," *SenSys*, pp. 154–165, 2005.

[4] S. Mintchev, R. Ranzani, F. Fabiani, and C. Stefanini, "Towards docking for small scale underwater robots," *Autonomous Robots*, 2014.

[5] G. Antonelli, *Underwater Robots*, ser. Springer Tracts in Advanced Robotics. Berlin, Heidelberg: Springer Berlin Heidelberg, 2014, vol. 2.

[6] T. I. Fossen, *Handbook of Marine Craft Hydrodynamics and Motion Control*, 1st. Trondheim: Wiley and son, 2011.

[7] J. W. Kamman and R. L. Huston, "Modelling of submerged cable dynamics," *Computers and Structures*, vol. 20, no. 1-3, pp. 623–629, 1985.

[8] Kamman and Huston, "Multibody dynamics modeling of variable length cable systems," *Multibody System Dynamics*, vol. 5, no. 3, pp. 211–221, 2001.

[9] H. Zhang and S. Wang, "Modelling and analysis of an autonomous underwater vehicle via multibody system dynamics," in *Proceedings of the 12th IFToMM World Congress*, Besancon, 2007, pp. 1–6.

[10] Yang Ke, Wang Xuyang, Ge Tong, and Wu Chao, "A dynamic model of rov with a robotic manipulator using kane's method," *2013 Fifth International Conference on Measuring Technology and Mechatronics Automation*, pp. 9–12, 2013.

[11] K. Yang, X.-y. Wang, T. Ge, and C. Wu, "A dynamic model of an underwater quadruped walking robot using kane's method," *Journal of Shanghai Jiaotong University (Science)*, vol. 19, no. 2, pp. 160–168, 2014.

[12] J. Park and N. Kim, "Dynamics modeling of a semi-submersible autonomous underwater vehicle with a towfish towed by a cable," *International Journal of Naval Architecture and Ocean Engineering*, vol. 7, no. 2, pp. 409–425, 2015.

[13] M. C. Nielsen, M. Blanke, and I. Schjølberg, "Efficient modelling methodology for reconfigurable underwater robots," in *To Appear: 10th IFAC Conference on Control Applications in Marine Systems*, Trondheim: International Federation of Automatic Control, 2016, pp. 1–7.

[14] F. E. Udwadia and P. Phohomsiri, "Explicit poincaré equations of motion for general constrained systems. part i. analytical results," *Proceedings of the Royal Society A: Mathematical, Physical and Engineering Sciences*, vol. 463, no. 2082, pp. 1421–1434, 2007.

[15] F. E. Udwadia and A. D. Schutte, "A unified approach to rigid body rotational dynamics and control," *Proceedings of the Royal Society A: Mathematical, Physical and Engineering Science*, vol. 468, no. 2138, pp. 395–414, 2012.

[16] K. Klausen, T. I. Fossen, T. A. Johansen, and A. P. Aguiar, "Cooperative path-following for multirotor uavs with a suspended payload," in *2015 IEEE Conference on Control Applications (CCA)*, IEEE, 2015, pp. 1354–1360.